Self-adaptive coupling frequency for unsteady coupled conjugate heat transfer simulations

Chai Koren, Ronan Vicquelin, Olivier Gicquel

▶ **To cite this version:**

Chai Koren, Ronan Vicquelin, Olivier Gicquel. Self-adaptive coupling frequency for unsteady coupled conjugate heat transfer simulations. International Journal of Thermal Sciences, 2017, 118, pp.340 - 354. 10.1016/j.ijthermalsci.2017.04.023 . hal-01744477

HAL Id: hal-01744477
https://hal.science/hal-01744477

Submitted on 27 Mar 2018

HAL is a multi-disciplinary open access archive for the deposit and dissemination of scientific research documents, whether they are published or not. The documents may come from teaching and research institutions in France or abroad, or from public or private research centers.

L'archive ouverte pluridisciplinaire **HAL**, est destinée au dépôt et à la diffusion de documents scientifiques de niveau recherche, publiés ou non, émanant des établissements d'enseignement et de recherche français ou étrangers, des laboratoires publics ou privés.

Self-adaptive coupling frequency for unsteady coupled conjugate heat transfer simulations

Chai KOREN[a,b,*], Ronan VICQUELIN[b], Olivier GICQUEL[b]

[a] *Air Liquide, Centre de Recherche Paris-Saclay, 1 Chemin de la Porte des Loges, 78350, Les-Loges-en-Josas, France*
[b] *Laboratoire EM2C, CNRS, CentraleSupélec, Université Paris-Saclay, Grande Voie des Vignes, 92295 Chatenay-Malabry cedex, France*

Abstract

Tackling transient conjugate heat transfer with high-fidelity methods such as large-eddy simulation (LES) requires to couple the LES solver with a heat transfer solver in the solid parts of the computational domain. Challenges include performance scalability, numerical stability and accuracy. In such unsteady simulations, both solvers integrate their respective set of equations in time independently for the sake of computational efficiency, and during a physical time corresponding to a coupling period to be specified. During the separate temporal integrations, the thermal state at the wall interface is typically set as a Dirichlet condition in the flow solver while a Neumann condition is imposed in the heat transfer solver to enhance numerical stability. When carefully validated, the chosen value of the coupling period which optimal value is initially unknown can be compared *a posteriori* with a refined solution. However, this optimal value of the coupling period (neither too large to remain accurate nor too short not to penalize the computational cost) is case-dependent.

In this study, an approach to automatically adapt the coupling period is presented. It relies on a describing the temporal evolution of the boundary temperature in hybrid cells composed of the neighboring fluid and solid mesh cells. Then, between coupling iterations, each solver advances separately with the same Dirichlet boundary condition on the computed interface temperature. Yielding a first order Ordinary Differential Equation (ODE) for the boundary temperature, the method allows using automatic adaptation of the step size to control the numerical integration error based on a prescribed tolerance by using controllers.

The coupling method is studied on 1D unsteady configurations where the results demonstrate that this energy conserving method is able to determine the coupling period automatically and efficiently for different configurations. The impact of excitation frequency and prescribed tolerance enables to select a specific PID controller which remains robust in spite of not carrying out step rejections for the sake of computational performance in the context of an LES application.

Keywords: Conjugate Heat Transfer, Coupling, Time step control

*Corresponding author
Email address: chai.koren@centraliens.net (Chai KOREN)

Nomenclature

Roman symbols

a	$\lambda/(\rho c_p)$, Thermal diffusivity
b	$\sqrt{\lambda \rho c_p}$, Thermal effusivity
c_p	Thermal capacity at constant pressure
f	Frequency
F	Thickening factor
G	a_f/a_s, Ratio of thermal diffusivities
H	Enthalpy
K	b_f/b_s, Thermal activity ratio
t	Time
T	Temperature
V	Cell volume
x	First space coordinate
Y_c	Progress variable

Greek symbols

Δt	Time step size
ϵ	Numerical integration error
η	Numerical tolerance
λ	Thermal conductivity
ϕ	Face-averaged flux
Φ	Face-integrated flux
ρ	Density
$\dot{\omega}$	Reaction rate
ω	Pulsation

Subscript

$_f$	Fluid domain value
$_s$	Solid domain value
$_{hyb}$	Hybrid cell value
$_{opt}$	Optimal value
$_{cpl}$	Coupling value
$_{[k]}$	Numerical value computed with an integration method of order k
$_{ext}$	External imposed conditions

Superscript

^{n}	Value taken at time $t = t_n$
$\overline{()}$	Mean value
$\widehat{}$	Numerical estimation of mean value
$'$	Fluctuating contribution

Abbreviation

DNS	Direct Numerical Simulation
LES	Large Eddy Simulation
RANS	Reynolds-Averaged Navier-Stokes equations
CHT	Conjugate Heat Transfer
ODE	Ordinary Differential Equation
RMS	Root Mean Square value
PID	Proportional-Integral-Derivative controller

1. Introduction

Context

Industrial applications are constantly growing in size and power and undergo more and more extreme conditions in terms of levels of pressure and temperature. It is therefore a key issue to accurately predict the wall heat flux distribution as early as possible in the design stage. Advanced methods such as Direct Numerical Simulations (DNS), when affordable, and Large-Eddy Simulations (LES) provide high-fidelity results and are becoming more and more popular in industrial applications. Thanks to the increasing confidence in Large-Eddy Simulation results, the range of applications is broadening to include multiphysics problems: In particular, several works [1, 2] have been carried out to characterize unsteady conjugate heat transfer (CHT) with high-fidelity approaches such as DNS or LES. In coupled multiphysics simulations, a partitioned approach is often retained where different numerical solvers are considered to treat the different physical phenomena. In numerical studies unsteady CHT, a flow solver and a solver solving the unsteady heat equation in the solid domain are considered. The coupling is carried out so that both solvers compute temporal iterations separately until a given physical time that corresponds to the prescribed coupling time step, also called coupling period. At these instants, data from both solvers are exchanged with each other, typically through MPI communications, in order to update their boundary conditions. The emergence of such detailed multiphysics calculations is very promising in order to reach high-fidelity predictions: temporal variations on the heat loads on the mechanical structure provide new valuable pieces of information.

The unsteady variations at the walls can be due to a transient following the starting (or shut down) of the system or a transient between two operating conditions. For a specific operating point with a turbulent flow, unsteady conjugate heat transfer also occurs because of the fluctuating heat loads generated by the turbulent flow. High-fidelity simulations of turbulent flows such as DNS or LES are the appropriate methods to capture the flow unsteadiness and the associated variable heat loads on the system. However, because of their computational costs, the simulated physical time with such approaches is limited (typically several seconds up to one minute at most in engineering applications). Thus, simulating low-cycle variations and slow transient is out of reach. This is also impractical because slow variations of the system conditions in respect to flow time scales can be treated in a quasi-steady approach. Therefore, unsteady CHT can be covered with DNS or LES to predict unsteady heat loads in transient regime or statistically steady turbulent flow as long as the physical time to simulate remains affordable. The transient time cannot then exceed several seconds typically while the fluctuations captured in steady regime are larger than 10 Hz.

First applications of such advanced methods to unsteady CHT problems have been related to nuclear engineering where thermal fluctuations in the solid material may lead to thermal fatigue. Kuhn *et al.* [1] have numerically investigated the mixing of hot and cold water streams in a T-junction. Resulting unsteadiness within the wall was characterized and analyzed in terms of root-mean-square and spectra of the wall temperature. Tiselj *et al.* [2] carried out DNS of a heated slab cooled with turbulent flow on both sides. The impact of the slab thickness and the material properties on the penetrating fluctuations of temperature within the slab was studied. A key parameter is the thermal activity ratio defined as the ratio of the fluid thermal effusivity and the solid one. When larger than unity, the temperature fluctuations in the flow are significantly impressed on the solid wall, yielding a strong thermal unsteadiness of the solid material.

In combustion applications, simulations of conjugate heat transfer with accurate methods such as LES are also recent [3, 4, 5]. Given the presence of hot temperature gases, these studies have first focused on predicting the mean thermal state of combustors' walls while retaining an approach appropriate to capture unsteady CHT details. Several phenomena in combustion applications require unsteady CHT studies which would be affordable with a LES approach. The transient heating of an aero-engine liner ($\approx$ 1-mm thick) only takes several seconds for example. However, when considering its interactions with its environment in the combustion chamber through fixations, the duration is larger and cannot be simulated with LES. Another example is during emergency procedure of a bi-engine helicopter in case of One-Engine-Inoperative (OEI) event where the additional power handled by the single remaining engine damages the gas turbine in less than a minute. The corresponding 30-Second and 2-Minute OEI ratings are optional ratings in the engine European certification. A final example is given with combustion instabilities which make the flame strongly unsteady with large variations in pressure and velocity. This can cause several issues [6] that either rapidly damage the system or result in premature component wear: Enhanced heat transfer and thermal stresses to combustor walls, oscillatory mechanical loads that result in low- or high-cycle fatigue of system components, and flame blowoff or flashback. In these phenomena, the combination of LES with CHT is a promising approach to address one of the fatigue contributions that is high-cycle fatigue due to unsteady heat loads.

The unsteady heat loads in combustion applications are induced by the flow which is gaseous. The corresponding activity ratio is very small while increasing moderately with pressure as $p^{1/2}$ for ideal gases. The resulting wall temperature fluctuations due to the flow variations are then quite damped in comparison to configurations with a larger activity ratio. However, since the temperature variations in combustion systems are of several hundreds Kelvins or even a couple of thousands Kelvins, the absolute level of wall temperature variations is not necessarily

negligible. This is even significant in extreme conditions as met in high-pressure hydrogen/oxygen flames whose transient flame-wall interaction has recently been studied numerically with transient CHT simulations of 1D head-on quenching [7].

Because the unsteady heat loads captured by large-eddy simulations of reactive flows can be of significant value, the motivation and ultimate goal of this work is to capture accurately such thermal variations within the solid parts of combustors. Nevertheless, let us outline that the coupling approach that is proposed is general and is not limited to the scope of such configurations.

Coupling time step

As already explained, a common approach to carry out multiphysics simulations is to couple several numerical solvers dedicated to each physical phenomenon. Each solver can therefore be optimized in terms of algorithms or data structure independently from the others. Another a priori simple approach consists in solving all sets of equations by the same numerical code [8, 2]. However, while ensuring continuity of the different considered fields, such an approach for unsteady CHT most often relies on explicit time integration for the sake of simplicity and is therefore penalized by small time stepping due to the most stringent phenomenon. This leads to a significant waste of computational resources due to one or several physical phenomena being over-resolved. For example, the time scale of heat conduction in a solid can be several orders of magnitude apart from the diffusion or convection time scales in a flow of gas or liquid. By considering separate solvers for each physics instead, each solver can retain an optimal number of time steps between coupling time steps. The issue is then to determine this coupling period. It is either arbitrarily chosen or, at best, the adequacy of the chosen value is verified in *a posteriori* tests [9, 3, 10]. Depending on the applications different values have been reported: For example, $3\,\Delta t_f$ in [4] or $50\,\Delta t_f$ in [5], where Δt_f is the flow solver time step. For the setting up of such complex simulations to mature, one should not leave free parameters to users when they can be determined. This will be achieved here thanks to the derived method.

The coupling period has also an impact on the computational cost and the temporal accuracy of the coupled simulation. With synchronized solvers, the flow and solid solver time steps fulfil the following constraint: $\Delta t_{cpl} = N_s \Delta t_s = N_f \Delta t_f$ where N_s and N_f are the number of iterations before exchanging data at the shared interface. While Δt_f is fixed internally by the flow solver, the number of solid solver iterations is typically set to one: $N_s = 1$. Let us give an order of magnitude of the corresponding computational cost in a practical coupled LES of a complex geometry[1]: Berger et al. [5] report a coupled CHT simulation compared to a flow simulation alone which costs 100,000 CPU hours. This computational time of the flow simulation corresponds to solving the Navier-Stokes equations in a reactive flow (with six additional transport equations for species) on a mesh of 15 million tetrahedral elements with an explicit second-order Lax-Wendroff scheme during 40 ms of physical time. The solid domain, where the heat conduction is solved, is meshed with five points in the liner thickness and is then made of 25 million tetrahedra. The solid heat transfer solver is coupled every 50 flow iterations with the LES where 864 cpu cores are attributed to the LES solver. In order to synchronize data exchange communications every 50 flow iterations, 160 cpu cores are attributed to the solid solver. These numbers provided in [5] enable to estimate the impact of the coupling frequency on the computational cost. Coupling every 50 flow iterations leads to a moderate 18% additional cost for the coupled simulation, which was the one retained by the authors. Coupling less frequently is even more affordable. On the other hand, coupling after each flow iteration would require 50x160= 8,000 cpu cores for the heat transfer solver (assuming an ideal parallel scalability of the solver) to synchronize data exchange communications 50 times sooner. This would lead to a computational time ≈10 times larger *i.e.* 1,000,000 CPU hours for the coupled simulation. Adding the burden of solving heat transfer in the solid after each LES time step solver is then impractical in large-scale simulations.
Regarding the impact on accuracy, the envisioned coupled LES captures the flow unsteadiness and associated variable heat loads. The accurate capturing of the corresponding varying wall heat flux and temperature depends on the size of the coupling time step: A large value might temporally under-resolved unsteady phenomena at the solid/flow interface.

Considering the key role of this quantity, the objective of this study is to derive a procedure to adapt the coupling period automatically. The necessity to adapt the time step to achieve accuracy/cpu work compromise is detailed in reference books on the numerical resolution of dynamic systems (see for example [11]). It is here applied to the simulation of unsteady conjugate heat transfer to determine the coupling time step. For large-scale applications: On the one hand, a smaller coupling time step is more costly and will yield a more accurate capturing of the simulated unsteady wall heat loads; On the other hand, a larger time step makes the coupled simulations cheaper but the temporal accuracy is reduced. The derived method determines the most appropriate coupling time step as a function of the desired accuracy. Two original benefits of the approach are then the removal of an arbitrary setting of the coupling period and the control of the compromise between accuracy and computational cost for the targeted multi-physics simulations using LES or DNS. In the un-

[1] The retained coupling procedure by Berger et al. [5] is not synchronized temporally. Nonetheless, by carrying out $N_s = 1$ steps in the solid solver between each coupling operations, their work is relevant here to illustrate the computational overhead of coupled simulations with a variable coupling period in synchronized approaches.

conventional case where N_s increases with Δt_{cpl} due to a fixed solid time step Δt_s smaller than the determined coupling period, the relative computational overhead of the coupled simulation is fixed and only saving in terms of exchanged data communications are achieved in addition to selecting an accurate Δt_{cpl}.

Boundary conditions for coupled solvers

For conjugate heat transfer simulations involving a flow solver coupled with a heat conduction solver, the computational domain is split into two sub-domains, fluid and walls. In the context of steady conjugate heat transfer, domain decomposition methods [12] provide the framework to couple the solid and fluid solvers. Well-known coupling methods such as Neumann-Dirichlet, Dirichlet-Dirichlet and Neumann-Neumann enable to iteratively converge towards the steady solution on the whole domain [13, 14, 15, 16, 17, 18].

For unsteady conjugate heat transfer, the solid and fluid solvers advance in time separately between coupling steps. Identical temperature and heat flux cannot then be maintained on both sides of the wall interface at all instants and one must deal with the discontinuity of temperature or heat flux at the fluid-solid interface. This issue highlights the need to correctly choose the boundary conditions used by the different codes at the shared boundary. Methods sharing the same terminology as their steady variant have then been derived.

Hence, a Dirichlet-Dirichlet coupling approach for unsteady conjugate heat transfer has been developed [19]: Each solver uses a prescribed boundary temperature as a Dirichlet condition, yielding different heat fluxes on both sides. After each coupling iteration, the boundary temperature is overwritten to ensure the boundary heat flux continuity. An analogous Neumann-Neumann coupling approach prescribes heat fluxes on both sides. During the coupling exchange, requiring the continuity of the boundary temperature yields a new heat flux value for the next coupling iteration. Due to some shortcomings with the numerical stability of the Dirichlet-Dirichlet and Neumann-Neumann approaches, a much-preferred approach is the Neumann-Dirichlet coupling [20, 21, 22, 23] to ensure the temperature continuity and heat flux conservation through the boundary at the discrete coupling steps: One solver is given a fixed temperature at the interface (Dirichlet condition) while the other one uses a Neumann condition with a given value of the wall heat flux. The interface boundary condition in each case is sent by the other code.

The work by Giles [24] has studied the stability of this Neumann-Dirichlet coupling. It was demonstrated that the stability of this kind of numerical coupling depends on the ratio $\rho_f c_f \Delta x_f / \rho_s c_s \Delta x_s$. As long as this ratio is less than unity, the Dirichlet boundary condition must be set to the flow solver while the wall heat transfer solver must use the Neumann boundary condition. As mentioned in the work of Giles [24], the aforementioned ratio is indeed below unity for gas-wall CHT applications. More recent studies have based their coupling methodology on such a Neumann-Dirichlet coupling [4, 25, 10, 26]. An issue encountered in some studies is the lack in energy conservation: Depending on the implementation of the boundary conditions, an energy deficit can occur and must be corrected [25].

Scope of the study

The literature review shows that the coupling period, *i.e.* the gap between solvers' communications, remains a parameter whose adequate value is not known *a priori* and is adjusted to each investigated configuration. To better tackle the issue of determining the compromise value of the coupling time step size, this study proposes a modified Neumann-Dirichlet coupling denoted as *Hybrid-cell Neumann-Dirichlet coupling*.

The Hybrid-cell Neumann-Dirichlet coupling for unsteady coupled conjugate heat transfer is presented in section 2, while section 3 deals with the numerical properties of the coupling: Validation, energy conservation and numerical stability. Finally, section 4 introduces the coupling time step size determination approach and a validation on a 1D coupled problem. Only 1D problems are here presented to allow a thorough study. Several choices of algorithms and implementations are nonetheless motivated by the final objective of this research which are unsteady conjugate heat transfer simulations using LES on parallel supercomputers.

2. Hybrid-cell Neumann-Dirichlet coupling for unsteady conjugate heat transfer

Unsteady conjugate heat transfer between a solid part and a fluid flow is treated by considering one simulation code for each domain: one for the fluid part, and one for the solid part. The two domains share a common boundary where both codes have to be coupled. The standard Neumann-Dirichlet approach yields algebraic coupling equations which do not allow for a direct method to automatically determine and adapt the coupling period. Time-adaptive algorithms, detailed in section 4, are available for ordinary differential equations (ODE). To take advantages of these algorithms, an ODE for the boundary temperature T_{bnd} is required. To do so, the evolution of T_{bnd} is obtained by writing a balance of energy on a hybrid-cell control volume made of two sub-volumes, one fluid and one solid. As detailed in this section, the boundary T_{bnd} is then updated over time using the wall heat fluxes of both solid and fluid codes. On the other hand, both codes use a Dirichlet boundary condition on the shared boundary, T_{bnd}. Let's outline that such a procedure is totally different from a Dirichlet-Dirichlet coupling [19], which is based on algebraic relations (heat flux continuity) to update the shared boundary and is limited by numerical instabilities. In fact, it is shown that the proposed coupling procedure retrieves the standard Neumann-Dirichlet correct behavior while enabling time step adaptation, hence the name

Hybrid-cell Neumann-Dirichlet coupling. This approach is detailed in the following section.

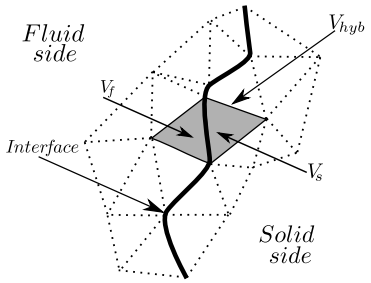

Figure 1: Fluid and solid domains used for a coupled simulation. Dashed triangles represent the cells (actual mesh cells for volume-centred formalism or dual mesh cells for vertex-centred formalism). Both grey triangles denote the fluid and solid cells of volume V_f and V_s respectively, which define the hybrid cell of volume V_{hyb} around the interface.

2.1. Derivation of the Hybrid-cell Neumann-Dirichlet coupling approach

The Hybrid-cell Neumann-Dirichlet coupling relies on a layer of hybrid cells at the boundary between the fluid and solid domains. As described in Fig. 1, each hybrid cell is composed of solid and fluid mesh cells on each side of the interface. Writing a balance equation for the hybrid cell's enthalpy, H_{hyb}, contained in cell volume V_{hyb} gives:

$$\frac{dH_{hyb}}{dt} = -\sum_{j=1}^{N_{face}} \boldsymbol{\phi}_j \cdot \mathbf{n}_{ext,j}\, A_j, \tag{1}$$

where N_{face} is the number of faces for the considered hybrid cell, A_j the $j-$th face area and $\mathbf{n_{ext,j}}$ is the normal vector pointing outwards for $j-$th face. The face-averaged fluxes $\boldsymbol{\phi}_j$ describe diffusive, convective or even radiative fluxes through the $j-$th face. For the sake of clarity, the flux integrated over all internal faces in the solid domain is denoted $\Phi_{s,bnd}$, and $\Phi_{f,bnd}$ in the fluid. Hence,

$$\frac{dH_{hyb}}{dt} = -\Phi_{s,bnd} - \Phi_{f,bnd}. \tag{2}$$

A first order approximation is made by taking the temperature inside the hybrid cell equal to T_{bnd}, the temperature value on the interface. Then, enthalpy being extensive, the temporal variation is split into the solid and fluid domain contributions, giving

$$\begin{aligned} \frac{dH_{hyb}}{dt} &= \int_{V_f} \rho_f c_{p,f} \frac{dT_{bnd}}{dt} dV_f \\ &+ \int_{V_s} \rho_s c_{p,s} \frac{dT_{bnd}}{dt} dV_s, \end{aligned} \tag{3}$$

where ρ_f and $c_{p,f}$ denote the density and specific thermal capacity at constant pressure in the fluid, and ρ_s and $c_{p,s}$ denote the same properties in the solid. Neglecting variations of thermo-physical properties inside each sub-domain in the hybrid cell, equation 3 becomes

$$\frac{dH_{hyb}}{dt} = \left(V_f \rho_f c_{pf} + V_s \rho_s c_{ps}\right) \frac{dT_{bnd}}{dt} \tag{4}$$

Finally, the temporal variation of the interface temperature is described by the following ordinary differential equation (ODE):

$$\frac{dT_{bnd}}{dt} = -\frac{\Phi_{f,bnd} + \Phi_{s,bnd}}{V_f \rho_f c_{pf} + V_s \rho_s c_{ps}} \tag{5}$$

The obtained equation can include an additional volume source term if necessary. Heat capacities and thermal conductivities involved in Eq. 5 can depend on temperature in general.

2.2. Numerical implementation of the Hybrid-cell Neumann-Dirichlet coupling

Unsteady conjugate heat transfer introduces the coupling time step parameter which is denoted by Δt_{cpl}. Here, it corresponds to the interval between each update of the boundary temperature value set to both solid and fluid solvers as boundary conditions. During a coupling iteration of duration Δt_{cpl}, each numerical code carries out one or more iterations independently with their own time step: Δt_s for the solid solver and Δt_f for the fluid solver. Hence, $\Delta t_{cpl} = N_s \Delta t_s = N_f \Delta t_f$, where N_s and N_f are the number of iterations within a coupling step for the solid and fluid solvers, respectively. The updating procedure for the boundary temperature is as follows:

- Both codes are at time t_n and have the same boundary condition $T_{bnd} = T^n_{bnd}$
- Each code advances independently from $t = t_n$ to $t_{n+1} = t_n + \Delta t_{cpl}$, while the boundary temperature is set to T^n_{bnd} during the entire time. The fluid solver code carries out N_f iterations while the solid solver completes N_s iterations.
- The integrated heat fluxes $\Phi_{s,bnd}$ and $\Phi_{f,bnd}$ required for the boundary temperature update are computed.
- Equation 5 is solved and yields the boundary temperature for time $t = t_{n+1}$, T^{n+1}_{bnd}

The Hybrid-cell Neumann-Dirichlet coupling approach requires the introduction of a third solver (see Fig. 2 a). This solver is a collection of ODE solvers for each hybrid cell between the solid and fluid mediums. It updates the temperature field at the boundary between both domains after each coupling iteration by solving Eq. 5. Coupling three solvers as depicted in Fig. 2 a would penalize significantly the parallel scalability of the conjugate heat transfer computation. Instead, the practical implementation of the Hybrid-cell Neumann-Dirichlet coupling is done by encapsulating the boundary solver within the flow and the

solid solvers according to Fig. 2 b in order to reduce the number of parallel communications. With such an implementation, the communication pattern is identical to the standard Neumann-Dirichlet approach, *i.e.* one array sent by each domain solver, and the method benefits from the corresponding programming optimizations [4, 27]. Let's outline that the exchange of flow and solid heat fluxes shown in Figure 2 b does not make the method similar to a Neumann-Neumann coupling since the received fluxes are used to solve Eq. 5.

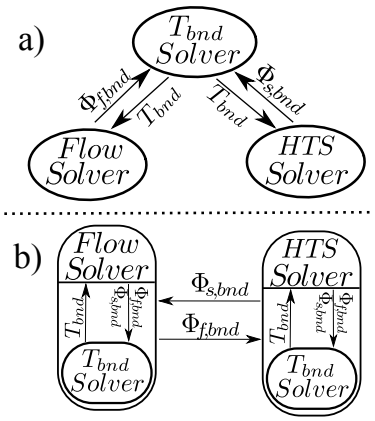

Figure 2: Scheme of the interface model for coupled unsteady conjugate heat transfer. a) Theoretical coupling procedure. b) Numerical implementation of hybrid-cell coupling: The boundary temperature solver is duplicated inside each physics solver. The flow solver and the solid heat transfer solver (HTS) exchange boundary fluxes, $\Phi_{s,bnd}$ and $\Phi_{f,bnd}$, and temperature, T_{bnd}, with the boundary solver which determines T_{bnd}.

Between two coupling steps, the flow and solid solvers carry out N_f and N_s inner iterations, respectively. The solvers' iterations yield then a group of discrete values $\Phi^i_{f,bnd}$ and $\Phi^j_{s,bnd}$, corresponding to the solver inner steps Δt^i_f and Δt^j_s. The total time averaged and face-integrated flux between two coupling steps is then given by the average value for the fluid side,

$$\begin{aligned}\overline{\Phi}_{f,bnd} &= \frac{1}{\Delta t_{cpl}} \int_{t_n}^{t_n+\Delta t_{cpl}} \Phi_{f,bnd} dt \\ &= \frac{1}{\Delta t_{cpl}} \sum_{i=1}^{N_f} \Phi^i_{f,bnd} \Delta t^i_f \end{aligned} \quad (6)$$

and similarly for the solid side.

Given the energy balance equation applied to the hybrid cell, the exact enthalpy change in the hybrid cell over the period Δt_{cpl} is:

$$\frac{\Delta H_{hyb}}{\Delta t_{cpl}} = -(\overline{\Phi}_{f,bnd} + \overline{\Phi}_{s,bnd}) \quad (7)$$

thus, the only time integration applied to the hybrid-cell and which ensures a strict energy conservation over the coupling period is the following first order explicit formula:

$$T^{n+1}_{bnd} = T^n_{bnd} - \Delta t_{cpl} \frac{\overline{\Phi}_{f,bnd} + \overline{\Phi}_{s,bnd}}{V_f \rho_f c_{pf} + V_s \rho_s c_{ps}} \quad (8)$$

Because of the independent evolution of each code, energy is only conserved at the end of a coupling step, once the boundary temperature has been updated using Eq. 8. Equation 8 is therefore the first order integration method used to numerically update the boundary temperature.

2.3. Comparison between Hybrid-cell Neumann-Dirichlet and Neumann-Dirichlet coupling approaches

It has been highlighted that the proposed approach is neither a Dirichlet-Dirichlet coupling nor a Neumann-Neumann coupling. This section shows that it is in fact very close to a Neumann-Dirichlet coupling in terms of numerical behavior. The improvement consists in enabling adaptation of the coupling time step which is detailed in Sec. 4.

Earlier studies showed that when coupling a flow solver with a solid heat transfer solver, a Neumann-Dirichlet coupling should be used for the sake of numerical stability [24]. This coupling method relies on applying a Dirichlet boundary condition in the flow solver and a Neumann boundary condition in the solid heat transfer solver at the interface between both mediums. The corresponding energy budget of the separate fluid and solid cells at the interface is represented in Fig. 3 (right). On the fluid side, the Dirichlet condition on the wall temperature yields an instantaneous equilibrated sum of fluxes on the fluid cell. Therefore, the face-integrated flux, Φ_w, sent to the solid heat transfer solver as a Neumann condition is identical to the previously defined quantity $\Phi_{f,bnd}$:

$$\Phi_w = \sum_{i \neq wall} \left(\boldsymbol{\phi}_{f,i} \cdot \mathbf{n}^{ext}_i \right) A_i = \Phi_{f,bnd}. \quad (9)$$

In the Neumann-Dirichlet approach, the wall temperature is then determined by the solid heat transfer solver as

$$\frac{dT_{bnd}}{dt} = -\frac{\Phi_w + \Phi_{s,bnd}}{V_s \rho_s c_{ps}} = -\frac{\Phi_{f,bnd} + \Phi_{s,bnd}}{V_s \rho_s c_{ps}} \quad (10)$$

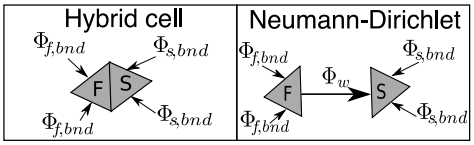

Figure 3: Energy budget in the hybrid cell approach (left) and in the Neumann-Dirichlet method (right). The fluid cell is denoted by F, respectively S for the solid cell. Φ_w is the flux sent by the flow solver to the solid solver in the Neumann-Dirichlet method.

The Hybrid-cell Neumann-Dirichlet coupling is compared to this result for the Neumann-Dirichlet coupling

method. When considering the conjugate heat transfer between a gas and a wall, $\rho_s c_{ps}$ is several orders of magnitude larger than $\rho_f c_{pf}$, which makes Eq. 5 similar to Eq. 10. Therefore, the Hybrid-cell Neumann-Dirichlet coupling is a generic coupling which behavior degenerates into the well-behaved Neumann-Dirichlet coupling behavior for gas-wall interaction. This physical asymmetry between both mediums is then retrieved by the proposed approach.

3. Numerical properties of the Hybrid-cell Neumann-Dirichlet coupling method

3.1. Validation using the Method of Manufactured Solutions

A numerical validation of the coupling is carried out by comparing numerical results to an analytical solution built using the Method of Manufactured Solutions ([28, 29]). This is done here on a two-layer 1D configuration with the primary goal of verifying that the Hybrid-cell Neumann-Dirichlet is able to correctly solve the physics at the boundary. Each 1D layer is governed by a 1D heat equation.

When obtaining an analytical solution is not easy such as in the present configuration, the Method of Manufactured Solutions enables to arbitrarily set the desired solution. An analytical source term is added to the considered equation to make the chosen function a solution of the problem, hence the name of *manufactured solution*. The chosen function, which would be here the temperature profile across both media, is assumed of class C^1. Unfortunately, this is not the case for the temperature because of the conductivity jump at the interface. Therefore, the method is here applied by first setting a C^1 heat flux profile. The imposed heat flux profile is

$$\phi^{mms}(x,t) = -cos(kx)e^{-\omega t} \tag{11}$$

where ω is a temporal pulsation and k a spatial wavenumber. Using the Fourier law, it is possible to determine the temperature gradient profile:

$$\frac{\partial T^{mms}}{\partial x}(x,t) = \frac{cos(kx)e^{-\omega t}}{\lambda(x)} \tag{12}$$

and, the conductivity λ is uniform in each sub-domain. The domain boundaries are located at $x = -L_1$ and $x = L_2$ which are given in Tab. 1, and the interface location is denoted by x_0. Considering a fixed temperature at $x = -L_1$, the analytical solution for the method of manufactured solutions can be obtained:

$$T^{mms}(x,t) - T^{mms}_{-L_1} = e^{-\omega t}\int_{-L_1}^{x} \frac{cos(kx)}{\lambda(x)}dx, \tag{13}$$

where

$$\begin{aligned}\int_{-L_1}^{x} \frac{cos(kx)}{\lambda(x)}dx &= \frac{sin(kx)}{\lambda(x)} + \frac{sin(kL_1)}{\lambda_1} \\ &+ H_{x_0}(x)sin(kx_0)\left(\frac{1}{\lambda_1} - \frac{1}{\lambda_2}\right)\end{aligned} \tag{14}$$

and $H_{x_0}(x)$ is the Heaviside function, such as $H_{x_0}(x) = 0$ if $x < x_0$ and $H_{x_0}(x) = 1$ otherwise. Injecting the temperature and heat flux functions inside the heat equation leads to:

$$\rho c_p \frac{\partial T^{mms}}{\partial t} = -\frac{\partial \phi^{mms}}{\partial x} + S^{mms}(x,t) \tag{15}$$

and the following analytical source term S^{mms}:

$$\begin{aligned}S^{mms}(x,t) &= ke^{-\omega t}sin(kx) \\ &- \frac{\rho c_p \omega}{k}\left[\frac{sin(kx)}{\lambda(x)} + \frac{sin(kL_1)}{\lambda_1}\right. \\ &+ \left. H_{x_0}(x)sin(kx_0)\left(\frac{1}{\lambda_1} - \frac{1}{\lambda_2}\right)\right]\end{aligned} \tag{16}$$

The method is applied to two coupled 1D layers, the computation parameters are given in Tab. 1. The configuration and corresponding boundary conditions are exhibited in Fig. 4. For the sake of this validation, the two codes are

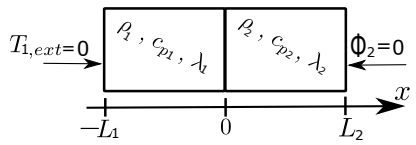

Figure 4: Studied 1D configuration using the MMS approach. Two media are present, of lengths L_1 and L_2. The outer boundary conditions are also mentioned.

coupled every iteration and the coupling time step is set to the time step value of medium 1, which corresponds to a Fourier number of $F = 0.1$. Both codes use the same spatial discretization step size. The outer boundary condition on the left side (medium 1) is a Dirichlet condition with $T^{mms}_{-L_1} = 0$ while the one used on the right side (medium 2) is a Neumann condition with $\phi = 0$. The temporal integration used is an explicit forward Euler and a centered second-order space discretization scheme. The results are

	Medium 1	Medium 2
ρ	10	200
λ	263	2000
C	50	200
N_{points}	300	300
Length [m]	0.005	0.005625
k	$4\pi/L_1$	-

Table 1: Parameters used for the MMS test case

plotted in Fig. 5. The numerical and analytical temperature spatial profiles collapse at the shown instant, validating the numerical model of the Hybrid-Cell Neumann Dirichlet approach.

3.2. Convergence order of the method

The test case described in the previous subsection is used here in order to verify the first order convergence of

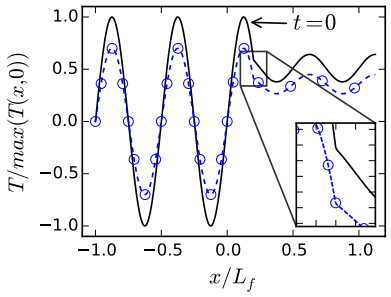

Figure 5: Spatial profiles of the temperature fluctuations scaled by the initial maximal temperature. Black plain line: Temperature at $t = 0$. Blue dashed line: Numerically computed temperature profile at $t = 25$ ms. Blue circles: Analytic manufactured solution at $t = 25$ ms.

the coupling method described by Eq. 8. The methodology for the test is the following:

- The 1D configuration and mesh are the same as in the previous section.
- The studied error is that of the interface temperature computed using the hybrid-cell.
- In order to isolate the error induced by the hybrid-cell coupling method, the numerical error produced individually by each code is minimized: The largest Fourier number (media #1) is set to 0.005 and both codes use a second order explicit time integration.

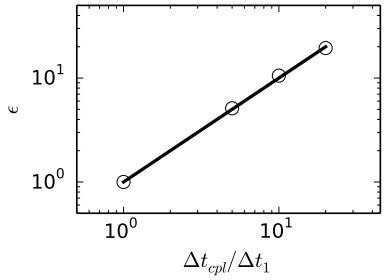

Figure 6: Scaled numerical error of the hybrid-cell computed interface temperature (ϵ) as a function of the coupling step size used. Black circles: Computed error values. Black plain line: Theoretical first order evolution.

The results of the study for different coupling time step sizes are plotted in Fig. 6. The numerical error is computed with the help of the reference solution obtained with the MMS approach. As shown by the obtained numerical results, the hybrid-cell coupling is indeed a first order temporal method.

3.3. Energy conservation

It was explained in the previous section that, for a strict energy conservation, the first order integration scheme Eq. 8 is needed. This scheme is compared to the first order forward Euler integration scheme,

$$T_{bnd}^{n+1} = T_{bnd}^{n} - \Delta t_{cpl} \frac{\Phi_{f,bnd}^{n} + \Phi_{s,bnd}^{n}}{V_f \rho_f c_{pf} + V_s \rho_s c_{ps}}, \qquad (17)$$

using the test case described in Sec. 4.2.1. Equation 17 is different from Eq. 8 where the average value $\overline{\Phi}_{f,bnd}$ on several fluid inner iterations is used instead of the instantaneous value $\Phi_{f,bnd}^{n}$. The comparison is done by monitoring the enthalpy residual R of the whole domain, defined as:

$$\begin{aligned} R(t) &= \int_{domain} \rho(x) c_p(x) T(x,t) dx \\ &+ \int_0^t (\phi_{f,ext} + \phi_{s,ext}) dt' \end{aligned} \qquad (18)$$

The first term in Eq. 18 is the sensible enthalpy of the entire domain at time t, while the second is the time integrated heat fluxes escaping from the outer boundaries of both media. $\phi_{f,ext}$ is the heat flux computed at the left (outer) boundary of the fluid medium while $\phi_{s,ext}$ is the one exiting from the solid medium. Each domain being solved with a conservative numerical scheme, the energy conservation through the medium interface is ensured, when the residual $R(t)$ is always null. Figure 7 shows the temporal evolution of $R(t)$ scaled by the entire domain absolute mean enthalpy $|\overline{H}|$. As seen in Fig. 7, the modified first order explicit integration scheme Eq. 8 is indeed strictly energy conserving as expected. On the other hand, the forward Euler scheme is not strictly energy conserving, though the energy lost over the plotted time lapse is very small. However, the energy deficit is clearly increasing over time, which could be an issue for long-duration simulations. In the following, Eq. 8 is always used as the first-order accurate integration scheme to enhance strict conservation. As shown in this section, the proposed coupling method ensures a strict energy conservation over a coupling step. Yet, this method is a loosely coupled approach [3] and not a strong coupling approach [30]. Strong

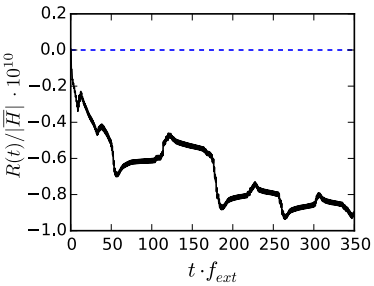

Figure 7: Temporal evolution of the domain enthalpy residual, R, scaled by the time-averaged enthalpy $\overline{H}$. Black plain line: First order explicit Euler from Eq. 17. Blue dashed line: Modified first order explicit integration scheme Eq. 8. Case conditions (see Sec. 4.2.1): $f_{ext} = 100$ Hz, $\eta = 5\,\%$ and PID controller.

coupling methods as addressed by Schwarz methods for domain decomposition [31, 32] are not considered here because of the unaffordable cost of global iterations. This choice is motivated since the method is to be applied to LES and DNS studies of unsteady conjugate heat transfer. Indeed, for the sake of computational efficiency, there is no iterative loop at the end of a coupling step which forces continuity for both temperature and heat flux. The result is that, between the boundary temperature and heat flux, only one can be imposed through a boundary condition for each code. The choice in this work is to impose a strict temperature continuity on the interface between the two domains and ensuring a strict energy conservation over a full coupling period.

3.4. Numerical stability analysis

The validation in Sec. 3.1 considered coupling at every iteration. This limitation is here elevated with a free coupling time step Δt_{cpl}. Each sub-domain (fluid or solid) then computes a given number of inner-iterations during a coupling step with its own integration time step. Thus, the fluid solver (respectively solid) computes N_f (respectively N_s) iterations using an inner time step Δt_f (respectively Δt_s), such as:

$$\Delta t_{cpl} = N_f \Delta t_f = N_s \Delta t_s. \tag{19}$$

The global stability of the coupling procedure is studied using the amplification matrix analysis by considering a joint temperature vector $\mathcal{T}$ of the solid and fluid domains' unknowns. It gathers the $n_f + 1$ fluid domain points $T_{f,1}, ..., T_{f,n_f}, T_{bnd}$ and the $n_s + 1$ solid domain points $T_{bnd}, T_{s,1}, ..., T_{s,n_s}$, where T_{bnd} is the shared boundary temperature. The temperature vector $\mathcal{T}$ is then defined as

$$\mathcal{T} = \left[T_{f,1}, ..., T_{f,n_f}, T_{bnd}, T_{s,1}, ..., T_{s,n_s}\right]^t, \tag{20}$$

The evolution of the temperature vector $\mathcal{T}$ between two coupling iterations is determined by the amplification matrix $\mathcal{M}_{hyb}$:

$$\mathcal{T}^{n+1} = \mathcal{M}_{hyb} \mathcal{T}^n \tag{21}$$

The amplification matrix is a block-matrix characterizing the interaction between the three solvers (fluid solver, coupling approach, solid solver). The spectral radius $\rho(\mathcal{M}_{hyb})$ of the matrix $\mathcal{M}_{hyb}$ determines the stability of the discretization operator [33, 34]. Indeed, the requirement for a stable scheme is:

$$\rho(\mathcal{M}_{hyb}) \leq 1 \tag{22}$$

The numerical stability of the coupling approach is here studied considering one unsteady heat equation solved in each domain d ($d = f$ or $d = s$),

$$\frac{\partial T_d}{\partial t} = a_d \frac{\partial^2 T_d}{\partial x^2}, \tag{23}$$

using forward Euler and second-order space discretization, which leads to the well-known discretized form

$$T_{d,i}^{n+1} = T_{d,i}^n + \mathcal{F}_d \left(T_{d,i-1}^n - 2T_{d,i}^n + T_{d,i+1}^n\right) \tag{24}$$

in each domain. $\mathcal{F}_d$ is the domain Fourier number,

$$\mathcal{F}_d = \frac{a_d \Delta t_d}{\Delta x_d^2}. \tag{25}$$

The numerical stability described by $\mathcal{M}_{hyb}$ is the result of the coupling procedure and of the retained numerical scheme in each domain. The latter is described by a domain-specific matrix $\mathcal{M}_d$ which represents a single inner iteration in a specific domain. With Eq. 24 and Dirichlet boundary conditions applied at the domain interface (T_{bnd} fixed according to the retained approach) and at the second extremity of the domain (for the sake of simplicity), the $(n_d + 1)$x$(n_d + 1)$ matrix $\mathcal{M}_d$ is given by

$$\mathcal{M}_d = \begin{bmatrix} 1 & & & & \\ \mathcal{F}_d & 1 - 2\mathcal{F}_d & \mathcal{F}_d & & \\ & & \ddots & & \\ & & \mathcal{F}_d & 1 - 2\mathcal{F}_d & \mathcal{F}_d \\ & & & & 1 \end{bmatrix}. \tag{26}$$

The interface flux for a domain d for a given inner-iteration k between the n^{th} and $(n+1)^{\text{th}}$ coupling steps is computed as:

$$\phi_{d,bnd}^{n,k} = -\lambda_d \nabla T_{bnd}^{n,k} \tag{27}$$

which can also be written as:

$$\phi_{d,bnd}^{n,k} = \mathcal{D}_{d,k} \cdot \mathcal{T}^n \tag{28}$$

where $\mathcal{T}^n$ is the temperature vector of the entire domain corresponding to the n-th time step, of shape $(n_f + 1 + n_s, 1)$, and $\mathcal{D}_{d,k}$ the line vector of shape $(1, n_f + 1 + n_s)$ corresponding to the boundary heat flux of medium d and the k-th internal substep. $\mathcal{D}_{d,k}$ is defined as:

$$\mathcal{D}_{d,k} = -\lambda_d \nabla_{bnd} \cdot \left(\mathcal{M}_d\right)^k \tag{29}$$

where $\left(\mathcal{M}_d\right)^k$, $\mathcal{M}_d$ to the power of k, is the matrix corresponding to the time integration using k substeps for medium d and ∇_{bnd} is the boundary gradient operator. Hence, the time averaged flux during the coupling iteration, used by Eq. 8, is obtained as:

$$\begin{aligned} -\overline{\nabla(\Phi)_{bnd}}^n &= \nabla_{bnd} \left(-\frac{\lambda_f}{N_f} \sum_{k_f=0}^{N_f-1} \left(\mathcal{M}_d\right)^{k_f} \right. \\ &+ \left. \frac{\lambda_s}{N_s} \sum_{k_s=0}^{N_s-1} \left(\mathcal{M}_s\right)^{k_s} \right) \mathcal{T}^n \end{aligned} \tag{30}$$

Therefore, $\mathcal{M}_{hyb}$ is defined as follows:

$$\mathcal{M}_{hyb} = \begin{bmatrix} \left(\mathcal{M}_f\right)_{[1:n_f-1]}^{N_f} & & 0 \\ & \dfrac{\overline{-\nabla(\Phi)_{bnd}}^n}{\sum_d \rho_d c_{p,d} V_d} & \\ 0 & & \left(\mathcal{M}_s\right)_{[2:n_s]}^{N_s} \end{bmatrix} \tag{31}$$

where $(\mathcal{M}_f)^{N_f}_{[1:n_f-1]}$ is a $(n_f - 1)$ x n_f matrix, equal to $(\mathcal{M}_f)^{N_f}$ without its last line. Thanks to $\mathcal{M}_{hyb}$ the spectral radius can be computed numerically. It is done for a fluid-solid couple made of Inconnel steel and oxycombustion burnt gases, used in the test case described in Sec. 4.2.1, and which thermal properties are given in Tab. 3. The coupling is considered stable if the spectral radius verifies $\rho(\mathcal{M}_{hyb}) \leq 1$. The corresponding stability map is plotted in Fig. 8 as a function of the solid domain Fourier number $\mathcal{F}_s$ and an hybrid Fourier number:

$$\mathcal{F}_{hyb} = \frac{\Delta t_{cpl}}{\rho_f c_{pf} \Delta x_f + \rho_s c_{ps} \Delta x_s} \left(\frac{\lambda_f}{\Delta x_f} + \frac{\lambda_s}{\Delta x_s} \right) \quad (32)$$

$\mathcal{F}_{hyb}$ can also be expressed using the Fourier numbers of each code, $\mathcal{F}_f$ and $\mathcal{F}_s$, and the number of iterations between two coupling steps, N_f and N_s:

$$\mathcal{F}_{hyb} = \theta N_s \mathcal{F}_s + (1 - \theta) N_f \mathcal{F}_f \quad (33)$$

where:

$$\theta = \frac{\rho_s c_{ps} \Delta x_s}{\rho_f c_{pf} \Delta x_f + \rho_s c_{ps} \Delta x_s} \quad (34)$$

The resulting stability map plotted in Fig. 8 is delimited

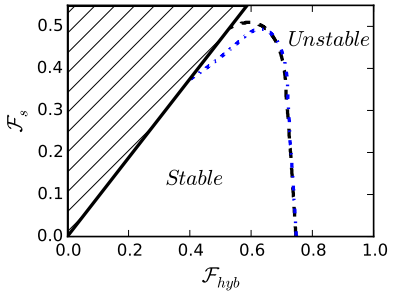

Figure 8: Stability regions of the hybrid-cell coupling as a function of the hybrid Fourier number, $\mathcal{F}_{hyb}$ and the solid maximal Fourier number $\mathcal{F}_s$. The hatched triangle corresponds to the zone where the coupling time step is smaller than the solid time step corresponding to $\mathcal{F}_s$, and hence $\Delta t_s = \Delta t_{cpl}$. Black dashed line: Second order spatial discretization. Blue dashed-dotted line: Fourth order spatial discretization. Black plain line: $\Delta t_s = \Delta t_{cpl}$.

on the top-left corner by the requirement $\Delta t_{cpl} \geq \Delta t_s$ and on the right side by a curve corresponding to $\rho(\mathcal{M}_{hyb})$ =1, here plotted for second-order and fourth-order spatial discretization. The hybrid Fourier number can be as high as 0.75 for moderate values of $\mathcal{F}_s$. On the limit $\Delta t_{cpl} = \Delta t_s$ corresponding to the lower edge of the top-left shaded triangle, the maximum solid Fourier number is 0.5 for the second-order space discretization, respectively 0.375 for the fourth-order discretization, which match the known stability criterion for a single-domain heat equation solved with forward Euler with the corresponding space discretization. Setting the solid Fourier number close to its stability limit ($\mathcal{F}_s \approx \mathcal{F}_s^{max} = 0.5$ for a second-order discretization), the stability is enhanced by setting $\mathcal{F}_{hyb}$ lower than an upper limit given by the intersection of the horizontal line $\mathcal{F}_s = \mathcal{F}_s^{max}$ with the curves in Fig. 8.

Considering $\Delta x_s = \Delta x_f$, $\theta \approx 1$ for typical gas-wall conjugate heat transfer. The hybrid Fourier number is then given by $\mathcal{F}_{hyb} = N_s \mathcal{F}_s$. For the sake of stability, the number of iterations N_s therefore remains small and is typically one. The corresponding number of fluid iterations $N_f = N_s (a_f \mathcal{F}_s)/(a_s \mathcal{F}_f)$ is proportional to the ratio of thermal diffusivities a_f/a_s which can attain several orders of magnitude for classical gas-wall interaction. The limited range of N_s makes the stability of the Hybrid-cell Neumann-Dirichlet coupling similar to the one for unsteady conjugate heat transfer in the solid using explicit methods. The stability limit in the coupling time step is then related to the solid conductive time scale based on the solid cell size. One possible choice could be to set the coupling time step to the maximum allowed value. Such value is small enough to describe accurately a slow transient of heat conduction in the solid. However, considering LES to compute this kind of phenomena is impractical (see context section in the introduction).

In the targeted unsteady CHT applications, LES resolves flow time scales that are smaller than the solid conductive time scale. Capturing the resulting unsteady loads in the solid accurately is not guaranteed by the stability criteria alone. Thus, requiring a given accuracy in the predicted wall temperature can lead to reduce the coupling time step below its critical stability value. The issue is then to determine a value of the coupling time step than enforces such an accuracy requirement.

4. Automatic determination of the coupling time step

As explained in Sec. 2, the coupling method analyzed in the previous section has been designed to yield an ordinary differential equation (Eq. 5) for the boundary temperature to allow a self-adaptation of the coupling time step. The latter desired feature is addressed in this section. Numerous ODE solvers determine a variable time step to adapt to the local stiffness of the problem and control the resulting numerical error [11]. Since the integration step size used to solve the boundary temperature equation corresponds to the coupling period, a control of the step size opens the path to an automatic determination of the coupling period in unsteady conjugate heat transfer simulations. The previous stability analysis of the coupling approach is very informative since it outlines the maximum allowed coupling time step. However, fulfilling the stability condition does not guarantee accuracy. Ensuring a given accuracy can require a more stringent limitation on the coupling time step, specifically for time-resolved unsteady CHT with LEs or DNS.

In this section, the retained method to estimate the numerical integration error is first presented. Then, different controllers for the time step size are introduced along with the concept of step rejection. Finally, test cases on

1D coupled simulations of conjugate heat transfer demonstrate that a PID controller is adequate even when no step rejection is performed.

4.1. Coupling time step determination algorithms

4.1.1. Step size determination with a generic control algorithm

The step size control algorithm is a control loop shown in Fig 9: After the boundary temperature is integrated, a test is carried out to compare the numerical integration error ϵ_n to the prescribed tolerance η. If the numerical error is low enough, the time step Δt_n is approved and the next step is then computed. On the other hand, if the error is too large, the time step is rejected and the integration is repeated with a smaller step Δt_{opt}. For the next step, the initial guess of the step size is chosen as equal to the previously accepted one. The determination of the new integration time step is explained in the following.

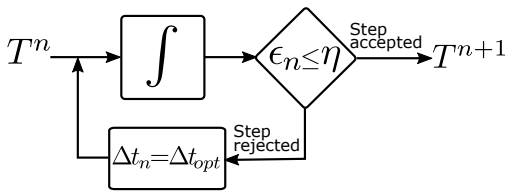

Figure 9: Generic control loop to advance the boundary temperature T^n to its value T^{n+1} with a numerical integration error ϵ_n below a given tolerance η by adapting the integration time step Δt_n.

4.1.2. Estimation of the numerical integration error

In order to determine the best time step to use, it is necessary to estimate the error of the integration scheme. The estimation is done with the help of two schemes of different orders. The numerical integration error at time t_n, for a method of order k is defined as:

$$\epsilon_n = |T^{n+1}_{[k]} - T(t_{n+1})| \tag{35}$$

where $T^n_{[k]}$ is the numerical approximation of order k at time t_n and $T(t_n)$ is the exact value. Since the value of the exact solution over time is not available, the numerical error is estimated by relying on a scheme of a higher order. Hence, introducing $T^n_{[k+1]}$, an approximation of $T(t_n)$ of order $k+1$, in the definition of ϵ_n:

$$\begin{aligned}
\epsilon_n &= |T^{n+1}_{[k]} - T(t_{n+1})| \\
&= |T^{n+1}_{[k]} - T^{n+1}_{[k+1]} + T^{n+1}_{[k+1]} - T(t_{n+1})| \\
&\leq \underbrace{|T^{n+1}_{[k]} - T^{n+1}_{[k+1]}|}_{O(\Delta t^{k+1})} + \underbrace{|T^{n+1}_{[k+1]} - T(t_{n+1})|}_{O(\Delta t^{k+2}) \ll O(\Delta t^{k+1})}
\end{aligned}$$

leads to the following estimation of the numerical integration error at each step for the scheme of order k

$$\epsilon_n \approx |T^{n+1}_{[k]} - T^{n+1}_{[k+1]}|. \tag{36}$$

The numerical error estimate requires solving the boundary temperature equation (Eq. 5) with numerical integration schemes of different order approximations. This equation being connected to the flow and solid solvers, implicit methods would require inner-iterations of the coupled flow and solid heat transfer simulations with the temperature updating procedure. Since unsteady CHT computations involving direct numerical simulations or large-eddy simulations are the target applications, implicit methods for the coupling process are deemed inadequate because of the necessity of supplemental communications and their iterative nature which lead to the re-computation of the current coupling time step along with the detailed simulations' inner time integration steps. Explicit integration methods are therefore preferred.

Given that previous values of boundary fluxes appearing in the right-hand-side of Eq. 5 are easily stored at each coupling period, Adams-Bashforth multi-step methods are selected. Consequently, the numerical error estimate in Eq. 36 is evaluated with the energy conserving first order approximation (Eq. 8) and the second order Adams-Bashforth formula (Eq. 38):

$$\begin{aligned}
f_{RHS} &= -\frac{\Phi_{f,bnd} + \Phi_{s,bnd}}{V_f \rho_f c_p + V_s \rho_s c_p} \\
T^{n+1}_{[1]} &= T^n + (t_{n+1} - t_n)\overline{f^n_{RHS}} \qquad (37) \\
T^{n+1}_{[2]} &= T^n + (t_{n+1} - t_n) f^n_{RHS} \\
&\quad + \frac{(t_{n+1} - t_n)^2}{2} \frac{f^n_{RHS} - f^{n-1}_{RHS}}{t_n - t_{n-1}} \qquad (38)
\end{aligned}$$

4.1.3. A first controller based on Taylor expansion

A simple step size control algorithm based on the Taylor expansion of the numerical solution is first presented. By definition, an integration scheme of order k verifies:

$$\begin{aligned}
T^{n+1}_{[k]} &= T(t_{n+1}) + \alpha_e (\Delta t_{n,cpl})^{k+1} \\
&\quad + o((\Delta t_{n,cpl})^{k+1})
\end{aligned} \tag{39}$$

between the instants t_n and $t_{n+1} = t_n + \Delta t_n$. Therefore, the numerical integration error ϵ_n can be estimated:

$$\epsilon_n \approx \alpha_e (\Delta t_{n,cpl})^{k+1} \tag{40}$$

Hence, if the aimed error value is η, its value can be linked to the value of the optimal time step size Δt_{opt}:

$$\eta = \alpha_e (\Delta t_{opt})^{k+1} \tag{41}$$

Combining equations 40 and 41 leads the following expression for the optimal time step size:

$$\Delta t_{opt} = \Delta t_{n,cpl} \left(\frac{\eta}{\epsilon_n} \right)^{1/(k+1)} \tag{42}$$

Equation 42 yields a variable time step. The associated variations can be troublesome by penalizing the dynamics

of the numerical resolution. This simple step size controller has been optimized in order to achieve higher smoothness of the responses and to reduce the number of rejected steps [35]. Noticing that Eq. 42 is similar to an I-controller, more advanced PI or PID ([11, 35]) controllers can be used instead.

4.1.4. PID controllers

Adopting the point of view of control theory to determine the optimal time step [11, 35], the following variables are introduced

$$\begin{aligned} C &= log(\Delta t_{cpl}) \\ \theta &= log(\epsilon) - log(\eta) \end{aligned} \tag{43}$$

where C is an actuator which influences θ, the variable to be controlled. The definition of θ is based on the numerical error ϵ and η the prescribed error tolerance. A general PID (Proportional-Integral-Derivative) controller will express the variation of C as

$$-\dot{C}(t) = K_P\dot{\theta}(t) + K_I\theta(t) + K_D\ddot{\theta}(t) \tag{44}$$

where K_P, K_I and K_D are respectively the proportional, integral and derivative control gains. Equation 44 can be solved analytically with the help of finite differences [11], which leads to:

$$\Delta t_{opt} = \Delta t^n_{n,cpl} \left(\frac{\eta}{\epsilon_{n-1}}\right)^{-\alpha} \left(\frac{\eta}{\epsilon_n}\right)^{\beta} \left(\frac{\eta}{\epsilon_{n-2}}\right)^{\gamma} \tag{45}$$

and

$$\alpha = K_P + 2K_D,\ \beta = K_P + K_I + K_D,\ \gamma = K_D \tag{46}$$

Equation 45 determines the next coupling time step from the numerical error of previous steps. The values of K_P, K_I and K_D are chosen in order to obtain the best precision and the smoothest evolution of the time step size [36, 35, 37]. The retained values are given in Table 2 for the three types of controllers considered: I, PI and PID. The PI controller gain coefficients are the ones originally published by Gustafsson [37], while the chosen PID controller is a member of the H312 family [36]. The automatic determination of the time step with error control also guarantees the stability of the numerical resolution. Indeed, numerical instabilities lead to larger numerical integration errors which then lead to a reduction of the integration time step by the controller [11]. The determined coupling time step will then be lower than the one prescribed by the stability constraint detailed in Sec. 3.4.

4.2. Validation of the interface model with determination of the coupling time step

The automatic time step control is tested with the help of a 1D heat-diffusion code. The code uses a finite-volume formalism and fourth order spatial discretization. Since the methodology is ultimately meant to be applied to an explicit LES/DNS solver, only explicit time integrations are considered. For the sake of simplicity, only the first order forward Euler time integration is used here.

Controller	$\alpha(k+1)$	$\beta(k+1)$	$\gamma(k+1)$
I	0	1	0
PI	0.4	0.7	0
PID	1/9	1/18	1/18

Table 2: *Controllers I, PI and PID defined by their gain coefficients [36, 37] for an integration scheme of order k.*

4.2.1. Description of the 1D test setup

The configuration studied here is composed of two mediums: The burnt gases of oxycombustion at a 20-bars pressure on the one hand, and an Inconnel steel on the other hand. The properties of both mediums are given in table 3.

Inconnel steel		Burnt gases	
λ_s	11.7	λ_f	0.158
ρ_s	8510.0	ρ_f	3.65
$c_{p,s}$	439.0	$c_{p,f}$	1738

Table 3: Properties of both mediums considered in 1D test cases in SI units: Thermal conductivity, density, thermal capacity at constant pressure,

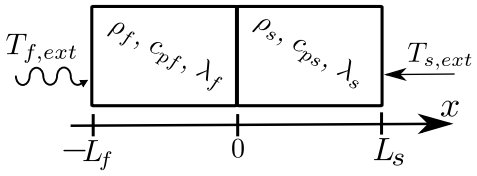

Figure 10: One-dimensional test case configuration. The length L_f of the fluid part is 1 mm while the length L_s of the solid part is 1 cm.

The test case consists of two coupled one-dimensional codes, each solving the unsteady heat equation in each medium. The configuration is shown in Fig. 10: the interface is located at the axial position $x = 0$ with the fluid medium on the negative x-values and the solid medium at the positive x-values. Boundary conditions are applied at both extreme edges of the domain: at $x = -L_f$, the fluid temperature fluctuates following a temporal sine wave of frequency f_{ext},

$$\begin{aligned} T_{f,ext} &= T(x = -L_f, t) \\ &= T_0(1 + 0.1\sin(2\pi f_{ext} t)) \end{aligned} \tag{47}$$

with $T_0 = 1000$ K, while at $x = L_s$, the solid's outer boundary $T_{s,ext}$ is a fixed temperature equal to the initial mean temperature in both mediums: 293 K.

The evolution of the resulting interface temperature along time is plotted in Fig. 11. The fluctuations amplitude is two orders of magnitude smaller than the one entering at $x = -L_f$. This effect can be attributed to the value

of the thermal activity ratio, which is equal to $4.78\,10^{-3}$ in this case. The reference solution was computed using a Laplace transform over the system of coupled equation, by combining a resolution in the Laplace-space, and the application of the inverse Laplace transform.

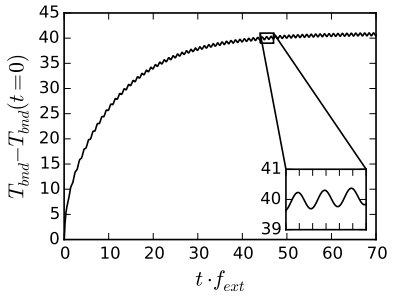

Figure 11: Temporal evolution of the boundary temperature for $f_{ext} = 100$ Hz.

4.2.2. Control with time step rejection

The three controllers presented in table 2 are compared considering step rejection: when the numerical error is not below the specified tolerance, the integration step used to update the temperature at the fluid-solid interface is rejected, meaning that it is restarted with a smaller time step given by Eq. 45. When the tolerance criterion is satisfied, the current step is accepted and the time step determined by Eq. 45 is used for the next step.

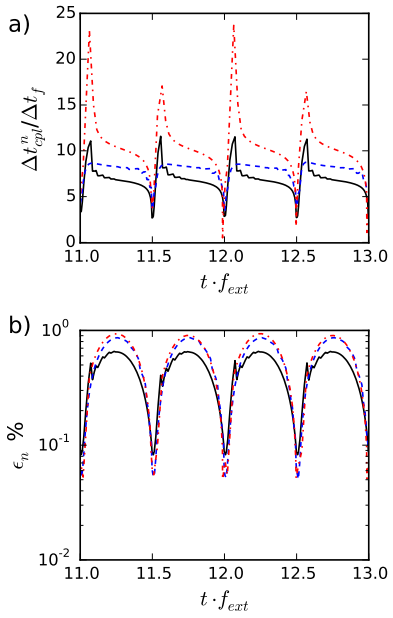

Figure 12: Evolution of the accepted coupling time step scaled by the fluid solver's time step (a) and corresponding numerical integration error (b) for different controllers: I (red dashed-dotted line), PI (blue dashed line) and PID (black plain line). Case conditions: $\eta = 1\%$ and $f_{ext} = 100$ Hz.

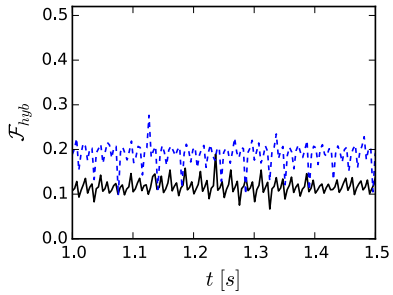

Figure 13: Temporal evolution of the hybrid Fourier number for the simulation controlled by a PID controller for two different tolerances. Black plain line: $\eta = 1\%$. Blue dashed line: $\eta = 3\%$. Case conditions: $f_{ext} = 100$ Hz.

Figure 12 shows the results for the three controllers with the tolerance $\eta = 1\%$ and the frequency $f_{ext} = 100$ Hz. In all three cases, the numerical error remains below the 1% prescribed tolerance. The numerical error used in this work is the L1 error :

$$\epsilon_n = |T^{n+1}_{[2]} - T^{n+1}_{[1]}| \tag{48}$$

The error and coupling time step are seen to evolve according to a frequency which is twice the one of the exterior perturbation. This is due to the absolute value in Eq. 36 which doubles the response frequency of the controller in comparison to the fluctuations' frequency. The evolution of the accepted step size is similar for the PI and PID controllers while the I controller presents much larger variations. As reported in Tab. 4, such variations of the step sizes determined by the I controller leads to a larger number of rejected time steps compared to the PI and PID controllers. In spite of such an ill behavior, the I controller provides the most efficient solution in terms of cost to precision ratio in this specific case.

Controller	I	PI	PID
Total number of steps	478	739	721
Number of rejected steps	113	38	31

Table 4: Comparison of the total number of coupling steps with the number of rejected steps for $\eta = 1\%$, $f_{ext} = 100$ Hz and a simulated time of 60 periods.

Figure 13 shows the temporal evolution of the hybrid Fourier number for two different tolerances, 1% and 3%. For both error tolerances, the obtained hybrid Fourier number is below the stability limit 0.375. As expected after explaining in Sec. 3.4 that the stability constraint is not enough to determine the coupling time step, an accuracy requirement can require a more stringent limitation in the coupling time step. Although this is here illustrate in a 1D test case, this automatic adaptation of the coupling period will enable to gain a significant control in the accuracy of unsteady CHT studies with LES or DNS without arbitrarily prescribing a value.

Considering that this approach is aimed to be used for 3D reactive simulations using LES or DNS the following issue arises: Rejecting multiple LES or DNS iterations of a flow solver is not affordable with the currently available computing resources. For the sake of optimal computational cost, tests are henceforth carried out without any rejection of the coupling time step. Hence, instead of closing the control loop, the optimal value for the n$^{\text{th}}$ coupling step size is used directly for the (n+1)$^{\text{th}}$ coupling step size:

$$\Delta t_{n+1,cpl} = \Delta t_{opt} \tag{49}$$

4.2.3. Control without time step rejection

In this section tests are conducted without rejection in order to compare all three controllers in terms of stability and efficiency. Figure 14 shows the fluctuating boundary temperature over time for a signal of $f_{ext} = 5$ Hz. The PI and PID controllers coincide on the reference solution while an instability occurs for the I controller due to a faulty time step control when non-optimal steps are not rejected. This issue was only encountered for the I-controller, and is due to the fact that it handles less efficiently perturbations than the PI or PID controllers [36]. For this reason the I controller is not considered stable enough and hence unsuitable for this usage. The rest of the study will only compare the PI and PID controllers.

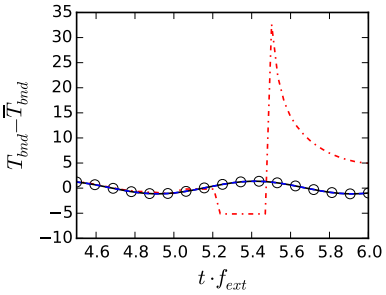

Figure 14: Temporal evolution of the difference of the boundary temperature T_{bnd} with its mean value, $\overline{T}_{bnd}$ for the reference solution (circles) and the I (red dashed-dotted line), PI (blue dashed line) and PID (black plain line) controllers. Case conditions: $\eta = 5$ % and $f_{ext} = 5$ Hz.

To differentiate the PI and PID controllers, it is interesting to study the ratio of coupling time step over fluid time step. The higher this ratio, the lower the coupling cost is, since it indicates a lower number of communications between solvers. Hence, the controller with highest ratio is the most cost efficient.

Figure 15 shows an example of deactivation of step rejection for the PI controller. It shows the instantaneous error (in log scale) of the boundary temperature computed using the interface model, as well as the ratio between coupling time step and fluid time step for a frequency of 100 Hz and $\eta = 0.1\%$. Unlike for the algorithm with step-rejection, in this case the numerical integration error can sometimes reach values larger than the prescribed tolerance. Nonetheless, the coupling step size is correctly adapted to keep this difference small.

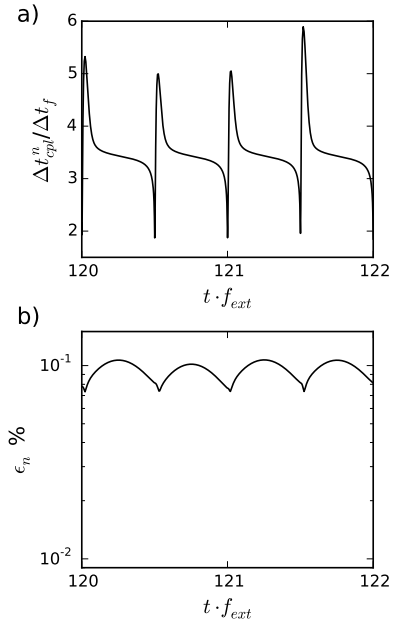

Figure 15: Evolution of the coupling time step scaled by the fluid time step (a) and the corresponding numerical integration error (b) computed by the PID controller without considering step rejection. Case conditions: $\eta = 0.1\%$ and $f_{ext} = 100$ Hz.

In order to characterize this behavior more quantitatively, the obtained average of the coupling time step and its root-mean-square (RMS) are compared for different imposed frequencies f_{ext} and tolerances η. The impact of these parameters on the computational cost due to solver coupling can then be assessed. Indeed, the higher the mean coupling time step is, the lower the computational cost is, and a smaller step size RMS also reduces the cost thanks to the removal of unnecessary fluctuations of the time step.

The influence of the error tolerance is first studied with a constant frequency of 100 Hz. The evolution of both mean and root mean square values of the ratio $\Delta t_{cpl}/\Delta t_f$ with η are plotted in Fig. 16 and Fig. 17, respectively.

As expected, the mean value of the coupling step size increases with the prescribed error tolerance. Moreover, it appears that the relation between both quantities follows

$$\Delta t^n_{cpl} = \beta \eta^b, \tag{50}$$

where $b = 1/2$ and β is independent of η, which is consistent with Eq. 41. Thus, for a given frequency, the instantaneous optimal value found for the coupling time step is proportional to the error tolerance to the power $1/(k+1)$ where k is the order of the numerical integration method. The mean value of the coupling time step is then also proportional to η^b. The value of $b = 1/2$ is consistent with the fact that the computed numerical integration error is that of a first order scheme.

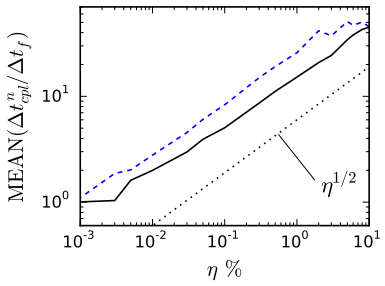

Figure 16: The mean coupling time step scaled by the fluid time step as a function of the prescribed tolerance η for the PI (blue dashed line) and PID (black plain line) controllers. The dotted line indicates a $\eta^{1/2}$-law for comparison. Case condition: $f_{ext} = 100$ Hz.

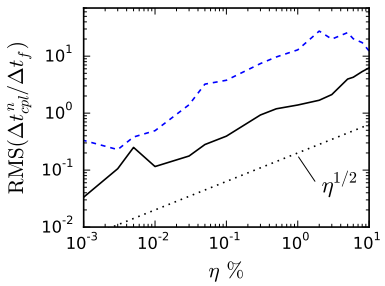

Figure 17: The root-mean-square (RMS) of the coupling time step scaled by the fluid time step as a function of the prescribed tolerance η for the PI (blue dashed line) and PID (black plain line) controllers. The dotted line indicates a $\eta^{1/2}$-law for comparison. Case condition: $f_{ext} = 100$ Hz.

Figure 17 shows that the RMS of the coupling step size has a similar behavior compared to the mean value. Equation 50 being valid instantaneously, the proportionality with $\eta^{1/2}$ remains valid for the RMS of the coupling step size. Yet, the RMS for the PI controller is much larger than for the PID controller, about an order of magnitude of difference. This high variance leads to a larger computational cost for the PI controller since very small time steps then need to be computed which leads to a higher number of coupling exchanges. The PID controller is then retained subsequently.

In figure 18, the influence of the frequency on the coupling step size is shown for three different error tolerances with the PID controller. As the frequency of the imposed fluctuations at $x = -L_f$ on the fluid side increases, the dissipation of the fluctuations in the fluid becomes more and more pronounced. The results are then shown with frequencies scaled by the fluid cut-off frequency f_c. f_c is here defined as the frequency for which only 1% of the imposed fluctuations amplitude would reach the distance L_f in a semi-infinite domain. It is then estimated analytically as $f_c = 25a_f/(\pi L_f^2)$, and for the considered test case: $f_c = 200$ Hz. For all three values of η (0.05%, 0.5% and 5%) shown in Fig. 18, the encountered behavior is the same: A first zone, for $f_{ext} \leq f_c$, where the coupling step decreases as f_{ext} increases, and then a second zone for $f_{ext} \geq f_c$ where the profiles of coupling step size flattens and then increases.

In the first zone, the slope indicates a f_{ext}^{-1}-law, which can be explained. For an integration method of order 1, a detailed Taylor expansion of the numerical integration error reveals that the proportionality factor in Eq. 41 is in fact linked to the second derivative of the boundary temperature:

$$\epsilon_n \propto \frac{\partial^2 T_{bnd}}{\partial t^2} (\Delta t^n_{cpl})^2 \tag{51}$$

When using the PID controller, the numerical integration error is close to the prescribed tolerance: $\epsilon_n \approx \eta$. Furthermore, the second order time derivative is proportional to f_{ext}^2. Therefore, the approximated coupling time step dependency on the f_{ext} is given by

$$\Delta t^n_{cpl} \propto \frac{\eta^{1/2}}{f_{ext}}, \tag{52}$$

which is the observed behavior.

In the second zone, the imposed frequencies are larger than the fluid domain cut-off frequency. Therefore, the fluctuations reaching the fluid-solid interface are below 1% and become smaller and smaller when f_{ext} increases. Hence, the boundary temperature behavior is closer and closer to a fixed boundary conditions that does not need to be resolved with finer coupling time steps to be computed accurately given the prescribed tolerance.

This section has showed that relying on the PID controller is necessary to minimize computational cost when step rejection is not affordable. Even though too large time

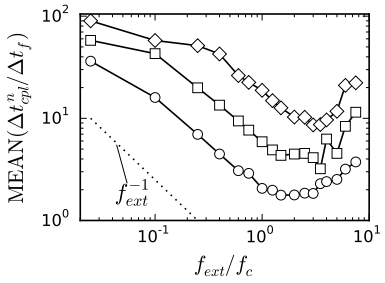

Figure 18: The mean coupling time step scaled by the fluid time step computed by the PID controller as a function of the frequency f_{ext} for different values of the prescribed tolerance η: 0.05% (line and circles), 0.5% (line and squares) and 5% (line and diamonds). The frequency is scaled by the fluid domain cut-off frequency $f_c = 25a_f/(\pi L_f^2) = 200$ Hz.

steps are not rejected, the controller showed sufficient robustness by adjusting the next steps accordingly in terms of accuracy and numerical stability.

5. Conclusion

When studying multiphysics heat transfer, a practical and accurate approach is to consider different numerical solvers for each phenomenon. Hence, for unsteady conjugate heat transfer, an unsteady flow solver is then coupled to an unsteady heat transfer solver in the solid domain. Previous works have considered different methodologies to couple these solvers (Neumann-Dirichlet or Robin-Dirichlet approaches) consistently. The typical issues that are addressed or still need to be solved are: the numerical stability of the coupling method or the lack of strict energy conservation. In particular, the coupling period, a key parameter in these simulations, is not known *a priori*. For large-scale applications with LES or DNS, it impacts the computational cost and accuracy of the simulation. This work introduces a coupling method named Hybrid-cell Neumann-Dirichlet to automatically determine this coupling period for unsteady conjugate heat transfer simulations. It is based on a prescribed threshold on the coupling method accuracy.

The coupling approach relies on a layer of hybrid cells on which an ordinary differential equation for the boundary temperature is solved using the wall heat fluxes provided by both flow and solid solvers. Dirichlet boundary conditions are then provided for the flow and solid heat transfer solvers. Several features (explicit time integration, no iterative procedure, ...) of the proposed coupling approach have been selected in agreement with the target applications which are coupled DNS/LES of unsteady CHT. Thanks to this formulation, the coupling approach is conservative over a coupling period and an automatic determination of the coupling time step is achieved by controlling the numerical integration error. The retained PID controller has been shown to remain robust and efficient even when no step rejection is carried out for the sake of computational performance. The control of the numerical error also ensures the numerical stability of the coupling procedure. The only parameter is then a prescribed tolerance to control the numerical accuracy of the coupling method.

This methodology has been validated on one-dimensional configurations and it has been demonstrated that the coupling time step adapts to the dynamics of each particular configuration, highlighting the interest of having an on-the-fly control of the coupling period. This self-adaptation of the coupling period is to be applied to high-fidelity unsteady conjugate heat transfer in future work with the use of multiphysics LES. Such simulations will benefit from the removal of an arbitrary setting of the coupling period and the control of the numerical accuracy. While initially motivated for combustion applications, the method is general. It can indeed also be of great interest in coupled CHT studies with a larger thermal activity ratio (than the one met with gaseous flows) which yield stronger coupling effects due to the more pronounced fluctuations of wall temperature.

The method still requires a mean to compute the permanent regime statistics. To do so, an artificial acceleration of the solid walls slow transient heating or cooling is usually retained to yield a reasonable computational cost. The proposed hybrid-cell approach will also need to address non-conformal meshes in the future.

Acknowledgment

This work was supported by the Air Liquide, CentraleSupélec and CNRS Chair on oxycombustion and heat transfer for energy and environment and by the OXYTEC project, grant ANR-12-CHIN-0001 of the French Agence Nationale de la Recherche. This work was granted access to the HPC resources of IDRIS under the allocations 2014-x20142b0164 and 2015-x20142b0164 made by GENCI.

References

[1] S. Kuhn, O. Braillard, B. Ničeno, H.-M. Prasser, Computational study of conjugate heat transfer in t-junctions, Nuclear Engineering and Design 240 (6) (2010) 1548–1557.

[2] I. Tiselj, J. Oder, L. Cizelj, Double-sided cooling of heated slab: Conjugate heat transfer dns, International Journal of Heat and Mass Transfer 66 (0) (2013) 781 – 790.

[3] F. Duchaine, A. Corpron, L. Pons, V. Moureau, F. Nicoud, T. Poinsot, Development and assessment of a coupled strategy for conjugate heat transfer with large eddy simulation: Application to a cooled turbine blade, International Journal of Heat and Fluid Flow 30 (6) (2009) 1129 – 1141.

[4] S. Jauré, F. Duchaine, G. Staffelbach, L. Gicquel, Massively parallel conjugate heat transfer methods relying on large eddy simulation applied to an aeronautical combustor, Computational Science and Discovery 6 (1) (2013) Article 015008.

[5] S. Berger, S. Richard, F. Duchaine, G. Staffelbach, L. Y. M. Gicquel, On the sensitivity of a helicopter combustor wall temperature to convective and radiative thermal loads, Applied Thermal Engineering 103 (2016) 1450–1459.

doi:http://dx.doi.org/10.1016/j.applthermaleng.2016.04.054.
URL http://www.sciencedirect.com/science/article/pii/S1359431116305403

[6] T. C. Lieuwen, Unsteady combustor physics, Cambridge University Press, 2012.

[7] R. Mari, B. Cuenot, J.-P. Rocchi, L. Selle, F. Duchaine, Effect of pressure on hydrogen/oxygen coupled flame–wall interaction, Combustion and Flame 168 (2016) 409–419. doi:http://dx.doi.org/10.1016/j.combustflame.2016.01.004.
URL http://www.sciencedirect.com/science/article/pii/S0010218016000134

[8] M. Shahi, J. B. Kok, J. R. Casado, A. K. Pozarlik, Study of unsteady heat transfer as a key parameter to characterize limit cycle of high amplitude pressure oscillations, in: ASME Turbo Expo 2014: Turbine Technical Conference and Exposition, American Society of Mechanical Engineers, 2014, pp. V05CT18A011–V05CT18A011.

[9] F. Duchaine, N. Maheu, V. Moureau, G. Balarac, S. Moreau, Large-eddy simulation and conjugate heat transfer around a low-mach turbine blade, Journal of Turbomachinery 136 (5) (2014) 051015.

[10] L. He, M. Oldfield, Unsteady conjugate heat transfer modelling, ASME Journal of Turbomachinery 133 (3) (2011) 031022.

[11] E. Hairer, S. Norsett, G. Wanner, Solving Ordinary Differential Equations I, Springer series in computational mathematics, 2008.

[12] A. Quarteroni, A. Valli, Domain decomposition methods for partial differential equations, no. CMCS-BOOK-2009-019, Oxford University Press, 1999.

[13] F.-X. Roux, J.-D. Garaud, Domain decomposition methodology with robin interface matching conditions for solving strongly coupled fluid-structure problems, International Journal for Multiscale Computational Engineering 7 (1) (2009) 29–38.

[14] A. Montenay, L. Paté, J. Duboué, Conjugate heat transfer analysis of an engine internal cavity, in: ASME Turbo Expo 2000: Power for Land, Sea, and Air, American Society of Mechanical Engineers, 2000, pp. V003T01A086–V003T01A086.

[15] A. Heselhaus, D. Vogel, H. Krain, Coupling of 3 d-navier-stokes external flow calculations and internal 3 d-heat conduction calculations for cooled turbine blades, AGARD, Heat Transfer and Cooling in Gas Turbines 9 p(SEE N 93-29926 11-07).

[16] W. D. Henshaw, K. K. Chand, A composite grid solver for conjuate heat transfer in fluid-structure systems, Journal of Computational Physics 228 (10) (2009) 3708 – 3741.

[17] A. Dorfman, Z. Renner, Conjugate problems in convective heat transfer: Review, Mathematical Problems in Engineering 2009.

[18] M.-P. Errera, S. Chemin, Optimal solutions of numerical interface conditions in fluid–structure thermal analysis, Journal of Computational Physics 245 (2013) 431 – 455.

[19] P. Abeloff, F. Dougherty, W. Van Dalsem, Thermal interaction between an impinging hot jet and a conducting solid surface, in: 8th AIAA Applied Aerodynamics Conference, Vol. 1, 1990.

[20] R. Voss, R. Sausen, Techniques for asynchronous and periodically synchronous coupling of atmosphere and ocean models, Climate Dynamics 12 (9) (1996) 605–614.

[21] F. Lunkeit, R. Sausen, J. M. Oberhuber, Climate simulations with the global coupled atmosphere-ocean model echam2/opyc part i: present-day climate and enso events, Climate Dynamics 12 (3) (1996) 195–212.

[22] R. E. Dickinson, Convergence rate and stability of ocean-atmosphere coupling schemes with a zero-dimensional climate model, Journal of the Atmospheric Sciences 38 (10) (1981) 2112–2120.

[23] U. Cubasch, K. Hasselmann, H. Höck, E. Maier-Reimer, U. Mikolajewicz, B. D. Santer, R. Sausen, Time-dependent greenhouse warming computations with a coupled ocean-atmosphere model, Climate Dynamics 8 (2) (1992) 55–69.

[24] M. B. Giles, Stability analysis of numerical interface conditions in fluid-structure thermal analysis, Iternational Journal for Numerical Methods in Fluids 25 (4) (1997) 421–436.

[25] E. Radenac, J. Gressier, P. Millan, Methodology of numerical coupling for transient conjugate heat transfer, Computers & Fluids 100 (2014) 95 – 107.

[26] L. He, Fourier spectral modelling for multi-scale aero-thermal simulations, International Journal of Computational Fluid Dynamics 27 (2) (2013) 118–129.

[27] F. Duchaine, S. Jauré, D. Poitou, E. Quémerais, G. Staffelbach, T. Morel, L. Gicquel, Analysis of high performance conjugate heat transfer with the openpalm coupler, Computational Science & Discovery 8 (1) (2015) 015003.

[28] P. J. Roache, Code verification by the method of manufactured solutions, Journal of Fluids Engineering 124 (1) (2002) 4–10.

[29] K. Salari, P. Knupp, Code verification by the method of manufactured solutions, Tech. rep., Sandia National Labs., Albuquerque, NM (US); Sandia National Labs., Livermore, CA (US) (2000).

[30] D. Estep, S. Tavener, T. Wildey, A posteriori error analysis for a transient conjugate heat transfer problem, Finite Elements in Analysis and Design 45 (4) (2009) 263 – 271. doi:https://dx-doi-org.bibliopam.ecp.fr/10.1016/j.finel.2008.10.011.

[31] A. Toselli, O. B. Widlund, Domain decomposition methods: algorithms and theory, Vol. 34, Springer, 2005.

[32] B. Smith, P. Bjorstad, W. Gropp, Domain decomposition: parallel multilevel methods for elliptic partial differential equations, Cambridge university press, 2004.

[33] C. Hirsch, Numerical computation of internal and external flows, vol. 1 fundamentals of numerical discretization, vol. 2 computational methods for inviscid and viscous flows (1988).

[34] G. Allaire, A. Craig, Numerical Analysis and Optimization: An Introduction to Mathematical Modelling and Numerical Simulation. Numerical Mathematics and Scientific Computation, Oxford University Press, 2007.

[35] K. Gustafsson, M. Lundh, G. Söderlind, A pi stepsize control for the numerical solution of ordinary differential equations, BIT Numerical Mathematics 28 (2) (1988) 270–287.

[36] G. Söderlind, Digital filters in adaptive time-stepping, ACM Transactions on Mathematical Software (TOMS) 29 (1) (2003) 1–26.

[37] K. Gustafsson, Control theoretic techniques for stepsize selection in explicit runge-kutta methods, ACM Transactions on Mathematical Software (TOMS) 17 (4) (1991) 533–554.